

Molecular photoacoustic imaging of angiogenesis with integrin-targeted gold nanobeacons

Dipanjan Pan,^{*,1,2} Manojit Pramanik,^{†,1} Angana Senpan,^{*} John S. Allen,^{*} Huiying Zhang,^{*} Samuel A. Wickline,^{*,†} Lihong V. Wang,^{†,2} and Gregory M. Lanza^{*,†}

^{*}Department of Medicine and [†]Department of Biomedical Engineering, Washington University School of Medicine, St. Louis, Missouri, USA

ABSTRACT Photoacoustic tomography (PAT) combines optical and acoustic imaging to generate high-resolution images of microvasculature. Inherent sensitivity to hemoglobin permits PAT to image blood vessels but precludes discriminating neovascular from maturing microvasculature. $\alpha_v\beta_3$ -Gold nanobeacons ($\alpha_v\beta_3$ -GNBs) for neovascular molecular PAT were developed, characterized, and demonstrated *in vivo* using a mouse Matrigel-plug model of angiogenesis. PAT results were microscopically corroborated with fluorescent $\alpha_v\beta_3$ -GNB localization and supporting immunohistology in *Rag1^{tm1Mom} Tg(Tie-2-lacZ)*182-Sato mice. $\alpha_v\beta_3$ -GNBs (154 nm) had 10-fold greater contrast than blood on an equivolume basis when imaged at 740 nm to 810 nm in blood. The lowest detectable concentration in buffer was 290 nM at 780 nm. Noninvasive PAT of angiogenesis using a 10-MHz ultrasound receiver with $\alpha_v\beta_3$ -GNBs produced a 600% increase in signal in a Matrigel-plug mouse model relative to the inherent hemoglobin contrast pretreatment. In addition to increasing the contrast of neovessels detected at baseline, $\alpha_v\beta_3$ -GNBs allowed visualization of numerous angiogenic sprouts and bridges that were undetectable before contrast injection. Competitive inhibition of $\alpha_v\beta_3$ -GNBs with $\alpha_v\beta_3$ -NBs (no gold particles) almost completely blocked contrast enhancement to pretreatment levels, similar to the signal from animals receiving saline only. Consistent with other studies, nontargeted GNBs passively accumulated in the tortuous neovascular but provided less than half of the contrast enhancement of the targeted agent. Microscopic studies revealed that the vascular constrained, rhodamine-labeled $\alpha_v\beta_3$ -GNBs homed specifically to immature neovasculature (PECAM⁺, Tie-2⁻) along the immediate tumor periphery, but not to nearby mature microvasculature (PECAM⁺, Tie-2⁺). The combination of PAT and $\alpha_v\beta_3$ -GNBs offered sensitive and specific discrimination and quantification of angiogenesis *in vivo*, which may be clinically applicable to a variety of highly prevalent diseases, including cancer and cardiovascular disease.—Pan, D., Pramanik, M., Senpan, A., Allen, J. S., Zhang, H., Wickline, S. A., Wang, L. V., Lanza, G. M. Molecular photoacoustic imaging of angiogenesis with integrin-targeted gold nanobeacons. *FASEB J.* 25, 000–000 (2011). www.fasebj.org

Key Words: *photoacoustics • molecular imaging • diagnostic imaging • gold nanoparticles*

THE CAPABILITIES OF ULTRASOUND have recently been expanded with laser optics to create an emergent hybrid modality, referred to as photoacoustic tomography (PAT) (1). PAT augments traditional ultrasound anatomical and Doppler flow information with high-resolution images of vasculature based on the detection of intrinsic optical absorbers (*e.g.*, hemoglobin). The method further affords estimates of hemoglobin oxygen saturation levels, differentiating venous from arterial blood (2–6). Briefly, PAT utilizes a short-pulse laser beam to elicit thermoelastic expansion of absorbers (such as proteins, hemoglobin, exogenous contrast agents), which then produce pressure waves [known as photoacoustic (PA) waves]. The PA waves received by a wideband ultrasonic transducer are used to reconstruct the 3-dimensional (3-D) tissue absorption distribution. Uniquely, PAT-based techniques overcome the resolution and depth restrictions of pure optical imaging, as well as the poor soft tissue contrast and speckle artifacts associated with ultrasound imaging.

Angiogenesis is an essential microanatomical component of tumor and cardiovascular progression that may be effective as a quantitative indicator of tumor or cardiovascular plaque progression or response to therapy (7–9). Although PAT generates high-resolution images of red blood cells in the microvasculature (10–17), hemoglobin imaging does not allow discrimination between immature neovasculature and mature microvessels without the adjunctive use of angiogenesis-specific molecular imaging agents. The objective of the present study was to develop, characterize, and demonstrate a vascular constrained, $\alpha_v\beta_3$ -targeted gold nanobeacon (GNB) for sensitive and specific discrimination

¹ These authors contributed equally to this work.

² Correspondence: D.P., Department of Medicine, Washington University School of Medicine, St. Louis, MO 63108, USA. E-mail: dpan@dom.wustl.edu; L.V.W., Department of Biomedical Engineering, Washington University School of Medicine, St. Louis, MO 63108, USA. E-mail: lhwang@seas.wustl.edu
doi: 10.1096/fj.10-171728

This article includes supplemental data. Please visit <http://www.fasebj.org> to obtain this information.

of immature angiogenic endothelial vessels from mature microvasculature.

MATERIALS AND METHODS

Materials

Unless otherwise listed, all solvents and reagents were purchased from Aldrich Chemical Co. (St. Louis, MO, USA) and used as received. Anhydrous chloroform was purchased from Aldrich and distilled over calcium hydride prior to use. Octanethiol-coated gold nanoparticles (2 to 4 nm) were purchased from Aldrich. Argon and nitrogen (UHP, 99.99%) were used for storage of materials. Spectra/Por membrane (cellulose, 20-kDa MWCO; Spectrum Medical Industries, Laguna Hills, CA, USA) was used for dialysis.

GNB synthesis

Octanethiol-coated gold nanoparticles (2–4 nm, 100 mg) in toluene were suspended in almond oil (4 ml), vortexed to homogeneity, and filtered through a small bed of cotton. The solvent was evaporated under reduced pressure at 45°C. The surfactant comixture included high-purity egg yolk phosphatidylcholine (91.9 mol%), cholesterol (8 mol%), and $\alpha_v\beta_3$ -peptidomimetic antagonist conjugated to PEG₂₀₀₀-phosphatidylethanolamine (0.1 mol%; Kereos, St. Louis, MO, USA). The surfactant comixture was dissolved in chloroform, evaporated under reduced pressure, dried in a 40°C vacuum oven overnight, and dispersed into water by probe sonication. This suspension was combined with the gold nanoparticle-suspended almond oil mixture (20% v/v), distilled deionized water (77.3% w/v), and glycerin (1.7%, w/v). The mixture was continuously processed at 20,000 psi for 4 min with an S110 Microfluidics emulsifier (Microfluidics, Newton, MA, USA) at 4°C. The GNBs were dialyzed against water using a 20-kDa MWCO cellulose membrane for a prolonged period of time and then passed through a 0.45- μ m Acrodisc syringe filter (Pall Life Sciences, East Hills, NY, USA). To inhibit lipid oxidation, the nanobeacons (NBs) were stored under an argon atmosphere, typically at 4°C.

The $\alpha_v\beta_3$ -integrin antagonist was a quinalone nonpeptide developed by Lantheus Medical Imaging (Billerica, MA, USA) and synthesized by Kereos (U.S. Patent 6,511,648 and related patents). The vitronectin antagonist was initially reported and characterized as the ¹¹¹In-DOTA conjugate RP478 and cyan 5.5 homologue TA145 (18). The specificity of the $\alpha_v\beta_3$ ligand mirrors that of the anti- $\alpha_v\beta_3$ -LM609 antibody (ref. 19; Chemicon International, Billerica, MA, USA), as assessed by staining and flow cytometry. The IC₅₀ for $\alpha_v\beta_5$, $\alpha_5\beta_1$, and GP IIb/IIIa was determined to be >10 μ M (Lantheus Medical Imaging; unpublished data).

Matrigel model of angiogenesis

Animal studies were performed under a protocol approved by the Washington University Medical School Animal Studies Committee. Athymic Nude-Foxn1tm (Harlan Laboratories, Indianapolis, IN, USA) with body weights ranging from 25 to 35 g were used. Anesthesia induction utilized a mixture of ketamine (85 mg/kg) and xylazine (15 mg/kg) that was maintained with 0.5–1% isoflurane in oxygen on a ventilator. GNBs were administered *via* tail vein at 2 μ l/g.

Matrigel (750 μ l; BD Biosciences, San Jose, CA, USA) enriched with fibroblast growth factor-2 (500 nm/ml; Sigma-Aldrich, St. Louis, MO, USA) and heparin (64 U/ml) was

implanted subcutaneously along the flank. PAT imaging was performed prior to treatment and serially over 5 h postinjection on d 16 and 17. Animals were randomly distributed into 4 groups and treated with $\alpha_v\beta_3$ -GNBs ($n=6$), $\alpha_v\beta_3$ -NBs without gold followed by $\alpha_v\beta_3$ -GNBs (competitive blockage; $n=2$), nontargeted GNBs (NT-GNBs; $n=3$), or saline ($n=2$).

PA imaging

A reflection-mode PA imaging system (Scheme 1 in ref. 20) was used for all PAT experiments. A tunable Ti:sapphire laser (LT-2211A; Lotis TII, Minsk, Belarus) pumped by a Q-switched Nd:YAG (LS-2137; Lotis TII) laser was the light source, providing <15-ns pulse duration and a 10-Hz pulse repetition rate. A dark-field ring-shaped illumination was used (21). The light energy on the sample surface was controlled to conform to the American National Standards Institute standard for maximum permissible exposure (22). A 10-MHz central frequency, spherically focused (2.54-cm focus length, 1.91-cm-diameter active area element, and 72% bandwidth) ultrasonic transducer (V308; Panametrics-NDT, Waltham, MA, USA) was used to acquire the generated PA signals. The signal was amplified by a low-noise amplifier (5072PR; Panametrics-NDT), and recorded using a digital oscilloscope (TDS 5054; Tektronix, Beaverton, OR, USA) with 50-MHz sampling. PA signal fluctuations due to pulse-to-pulse energy variation were compensated for signals from a photodiode (DET110; Thorlabs, Newton, NJ, USA), which sampled the energy of each laser pulse.

A linear translation stage (XY-6060; Danaher Motion, Radford, VA, USA) was used for raster scanning to obtain 3-D PA data. A computer controlled the stage and synchronized it with the data acquisition. To shorten the data acquisition time, a continuous scan was used without signal averaging. Typical scanning values were as follows: field of view, 14 \times 14 mm; voxel dimension, 0.1 \times 0.2 mm; laser pulse repetition rate, 10 Hz; acquisition time, \sim 24 min. *In vitro* phantom samples were placed in a degassed water bath (5 \times 5 cm) sealed beneath an optoacoustically transparent clear membrane. *In vivo* imaging was performed using ventilated anesthetized mice with shaved flanks, constantly warmed to 37°C and positioned immediately beneath the transparent clear membrane. Acoustic gel was used for improved ultrasound coupling.

Two parameters were calculated from the PAT images: the number of pixels of hemoglobin in blood vessels, and the PA signal amplitude in those pixels. An angiogenesis index was defined as the cross-product of blood vessel pixel number and total PA signal from those pixels. The data for each PA acquisition were normalized to the pretreatment (baseline) to create a normalized angiogenesis index of each animal.

Data were statistically analyzed using SAS (SAS Institute, Cary, NC, USA). General linear models were used to assess differences in angiogenic index between treatment groups. For ANOVA with significant *F* test, the least-square means procedure was utilized to examine differences ($P<0.05$) between the unequal group sizes. Data are reported as least-square means and the error of the least-square means.

Microscopy

Matrigel was implanted into a separate cohort of *Rag1^{tm1Mom}* Tg(TIE-2-lacZ)182-Sato mice (Jackson Laboratories, Bar Harbor, ME, USA) to assess localization of $\alpha_v\beta_3$ -GNB to nascent angiogenic endothelium (Tie-2⁻, PECAM⁺) *vs.* stabilized maturing microvessels (Tie-2⁺, PECAM⁺) (23, 24). Matrigel plugs were created as described above. On d 16, the mice were reanesthetized and administered rho-

damine-labeled $\alpha_v\beta_3$ -GNBs *via* tail vein injection. After 2 h, the animals were euthanized. The Matrigel plugs were excised and frozen in optimal cutting temperature (OCT) compound (Sakura Finetek, Torrance, CA, USA) for cryo-sectioning.

Frozen sections (10 μm) were studied with an Olympus BX61 microscope and a F-View II camera using a Cy3.3 filter (Olympus, Tokyo, Japan). The cell nuclei were counterstained with DAPI. Immunohistochemistry for endothelial PECAM-1 was performed on adjacent frozen sections (clone MEC13.3; BD Biosciences, San Jose, CA, USA) developed with ABC method and VIP substrate kits (Vector Laboratories, Burlingame, CA, USA) and counterstained with methyl green. Hematoxylin and eosin (H&E) staining was performed using routine histochemistry methods.

For Lac-Z staining of the Tie-2 receptor, 10- μm sections were fixed in 2% paraformaldehyde and 0.125% glutaraldehyde in PBS for 5 min. Fixative was aspirated, and the slides were incubated 3 times for 1 min each in 2 mM MgCl_2 in PBS. Slides were incubated 3 times for 2 min in a PBS mixture (50 ml) containing MgCl_2 (2 mM), 0.02% nonylphenoxypolyethoxyethanol (10 μl ; Nonidet P-40), and desoxycholate (5 mg). Subsequently, the slides were placed in staining buffer (<http://mammary.nih.gov/tools/histological/histology/index.html>) without 5-bromo-4-chloro-3-indolyl- β -D-galactopyranoside (X-gal) for 2 min followed by the addition of

X-gal overnight at 37°C. The sections were counterstained with nuclei fast red. Light images were captured with a ColorView II camera (Olympus).

RESULTS

As illustrated in **Fig. 1**, GNBs are colloidal nanoparticles with a phospholipid surfactant encapsulating 2- to 4-nm gold oleate particles suspended in vegetable oil. GNB hydrodynamic diameter, based on dynamic light scattering, was 159 ± 15 nm, with a ζ potential of -40 ± 09 mV. The particle height by atomic force microscopy was 95 ± 31 nm, reflecting modest flattening of the soft GNB particle against a hard surface. The gold content of the 20% (vol/vol) GNB colloidal suspension was 1080 $\mu\text{g/g}$ or 31,590 gold atoms/GNB. Each bound GNB particle incorporated 2289 gold nanoparticles. PA signal from GNBs was nearly 10-fold greater than blood on an equal volume basis, (see Supplemental Fig. A). Moreover, GNB PA signal (mV peak to peak) increased monotonically from a lower detection limit in PBS of 77

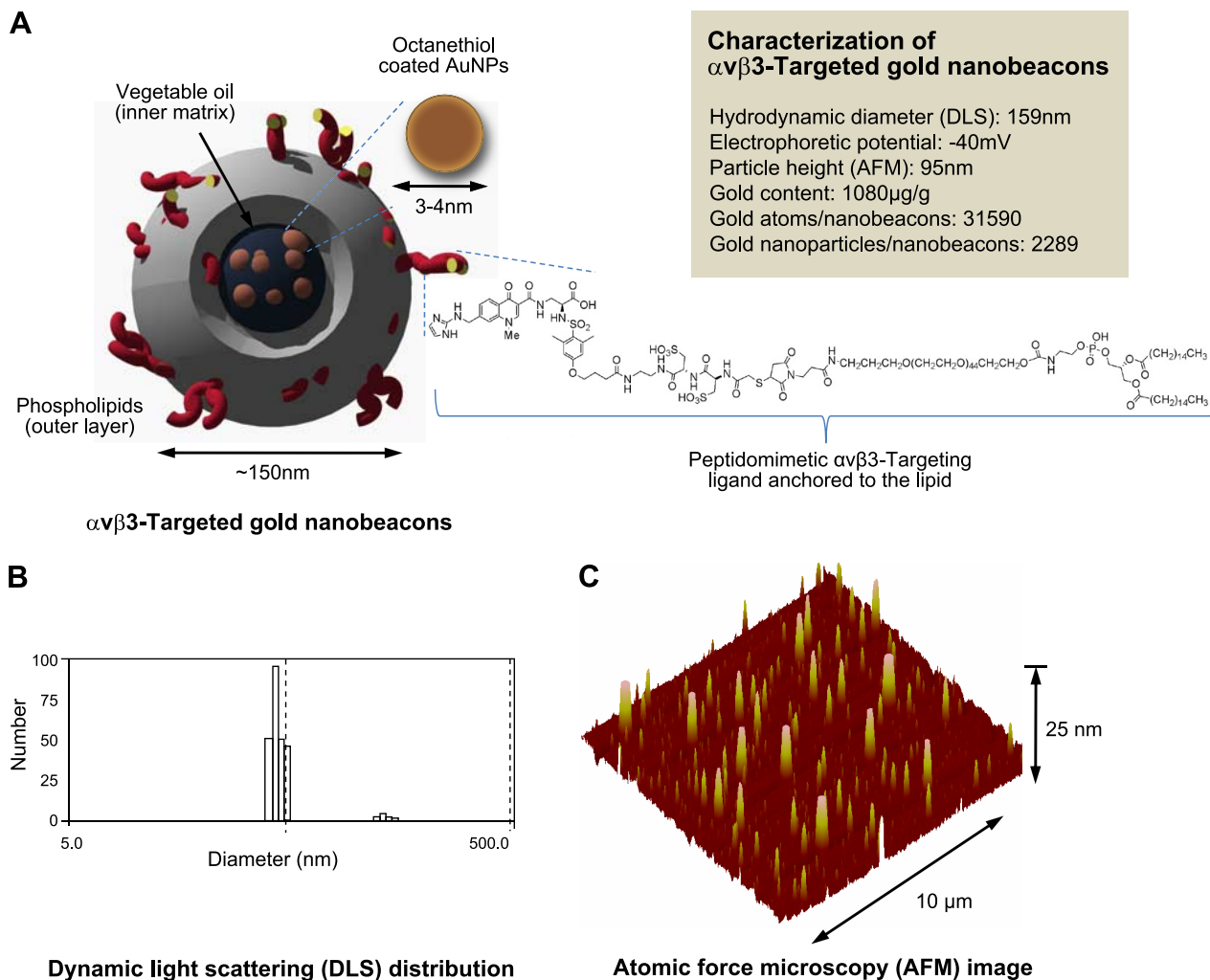


Figure 1. A) Targeted GNBs incorporating octanethiol-functionalized gold nanoparticles (AuNPs). $x = 1\text{--}2$ mol% phospholipid coating and presenting $\alpha_v\beta_3$ peptidomimetics on the surface. B) Dynamic light scattering (DLS) profile of targeted GNBs. C) AFM image of GNBs drop-deposited over glass surface. Average height $H_{av} = 95 \pm 31$ nm.

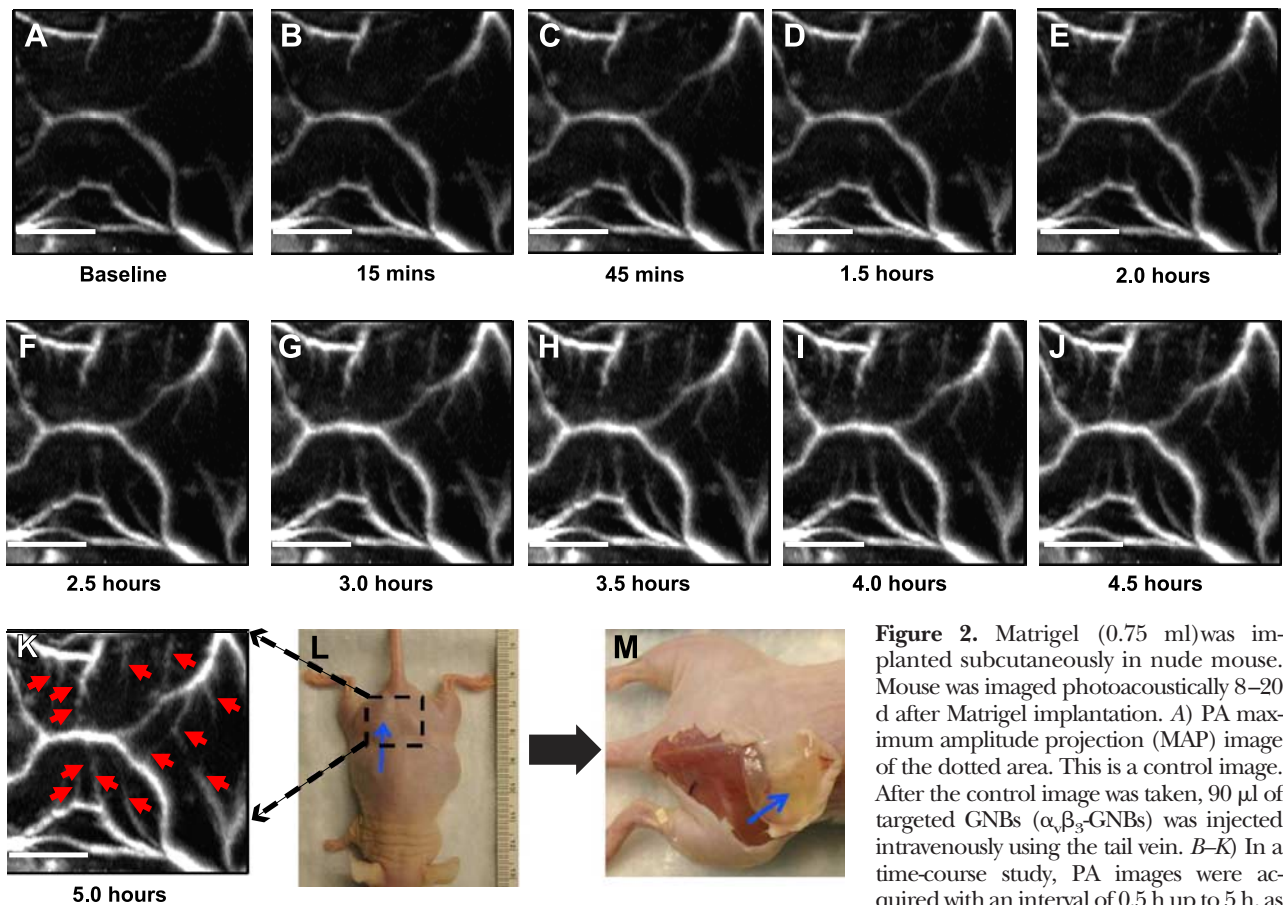


Figure 2. Matrigel (0.75 ml) was implanted subcutaneously in nude mouse. Mouse was imaged photoacoustically 8–20 d after Matrigel implantation. *A*) PA maximum amplitude projection (MAP) image of the dotted area. This is a control image. After the control image was taken, 90 μ l of targeted GNBs ($\alpha_v\beta_3$ -GNBs) was injected intravenously using the tail vein. *B–K*) In a time-course study, PA images were acquired with an interval of 0.5 h up to 5 h, as

indicated. Red arrows in 5-h postinjection PA image (*K*) point to the angiogenic sprout (not visible in *A*). *K*) For all PA images, $\lambda = 767$ nm; scale bar = 5 mm. *L*) Digital photograph of mouse implanted with Matrigel plug. Blue arrow points to the plug. Dotted area was imaged. Smallest tick on ruler = 1 mm. *M*) Digital photograph of the sacrificed mouse after all image acquisition. Skin was removed to show the Matrigel plug (blue arrow).

nM up to 5 μ M at near-infrared (NIR) wavelengths between 740 and 810 nm (see Supplemental Fig. A).

$\alpha_v\beta_3$ -GNBs were evaluated in a mouse Matrigel-plug model of angiogenesis. Mice bearing 16- to 17-d implants were intravenously treated with saline, $\alpha_v\beta_3$ -GNBs, $\alpha_v\beta_3$ -NBs, $\alpha_v\beta_3$ -NBs followed by $\alpha_v\beta_3$ -GNBs, or NT-GNBs. PA signal changes in the Matrigel plug were monitored serially over ≥ 5 h (**Fig. 2**). A time-course study revealed gradual enhancements with targeted GNBs posttreatment, at 15 min, 45 min, 1.5 h, and every 0.5-h interval thereafter until the 5-h time point. It is quite evident that with time, integrin-targeted GNBs penetrated deep into the Matrigel plug and bound the nascent vessels. The vessels that were seen in the Matrigel plug were angiogenic and still in development. The $\alpha_v\beta_3$ -GNBs enhanced both those with early blood flow and another subset where blood flow had not begun or was below PAT detection. Angiogenesis indexes, normalized to individual baseline images, increased steadily with time over the experiment among mice given $\alpha_v\beta_3$ -GNBs, while in the saline control treatment group, no changes in vascularity or contrast enhancement were appreciated (see Supplemental Fig. B). Average PA contrast enhancement measured in the $\alpha_v\beta_3$ -GNB mice was >6-fold (600%) relative to the saline control group and ~ 2 -fold (200%) more than

the NT-GNB group (**Fig. 3**). The relative difference in the magnitude of $\alpha_v\beta_3$ -targeted *vs.* nontargeted particles was consistent with previous measurements reported in cancer models (25, 26) and reflected the lower magnitude of contrast achievable through passive entrapment of nanoparticles in a tortuous neovasculature. *In vivo* competitive blockade of $\alpha_v\beta_3$ -GNBs with $\alpha_v\beta_3$ -NBs diminished the PA signal enhancement essentially equivalent to the saline-only response. PA signal in mice administered saline did not differ from pretreatment baseline contrast levels.

Figure 2 illustrates in native black-and-white PA images the marked enhancement of angiogenic vessel contrast over time. Individual microvessels observed prior to treatment were markedly enhanced with $\alpha_v\beta_3$ -GNBs. Remarkably, a pattern of neovascular bridges between neovessels and budding angiogenic sprouts was easily visualized with noninvasive PAT and $\alpha_v\beta_3$ -GNBs that could not be detected with hemoglobin alone. These developing neovessels were likely too immature and incomplete to support blood flow. Indeed, these images illustrate clearly the genesis of neovasculature in the Matrigel-plug model.

Microscopic characterization of the Matrigel PA imaging result was pursued using a separate cohort of *Rag1^{tm1Mom} Tg(TIE-2-lacZ)182-Sato* mice. Matrigel-plug

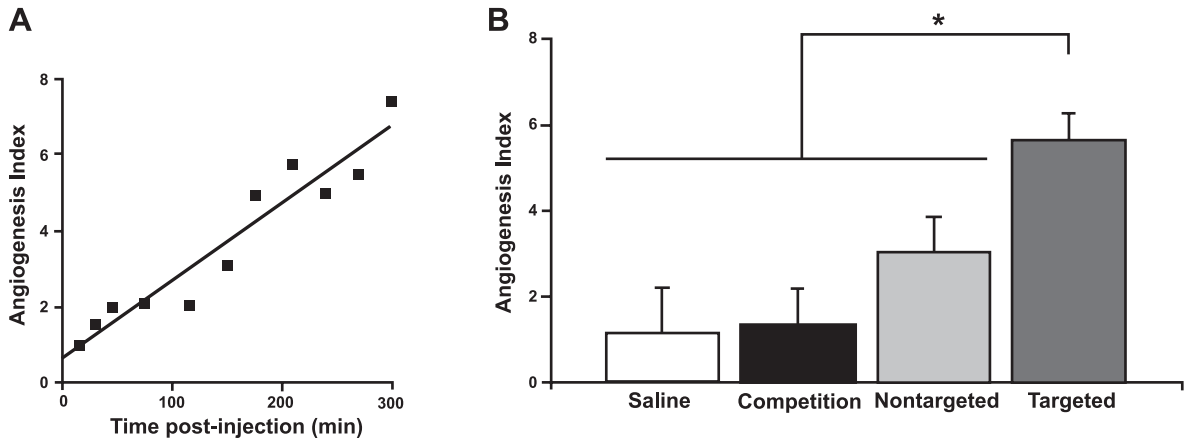


Figure 3. A) Angiogenesis index *vs.* time. B) Angiogenesis index (normalized) at 5 h postinjection for various cases. * $P < 0.05$.

angiogenesis was targeted with rhodamine-labeled $\alpha_v\beta_3$ -GNBs *in vivo*, and then the plug was excised for fluorescent and light microscopy visualization 2 h later (Fig. 4). Figure 4A presents a low-power H&E-stained example of an excised Matrigel plug with the muscle and skin labeled for orientation. The red box depicts a region of interest closely approximated to the perimeter of the Matrigel depot, which coincides with images in Fig. 4B–D. The blue box defines a nearby subcutaneous region of interest, which is also depicted in Fig. 4E–G. Fluorescent microscopy revealed the marked

accumulation of rhodamine $\alpha_v\beta_3$ -GNB nanoparticles in the immediate Matrigel periphery (Fig. 4B) that was not appreciated in the adjacent subcutaneous tissue (Fig. 4E). PECAM staining demonstrated abundant microvasculature in both the red (Fig. 4C) and blue (Fig. 4F) tissue regions. PECAM distribution in Fig. 4B was closely aligned with the targeted rhodamine $\alpha_v\beta_3$ -GNBs, but microvessels evident in Fig. 4F showed no decoration with rhodamine nanoparticles. Lac-Z staining, which was regulated by the Tie-2 promoter, was negligible in Fig. 4D, where $\alpha_v\beta_3$ -GNBs were prevalent.

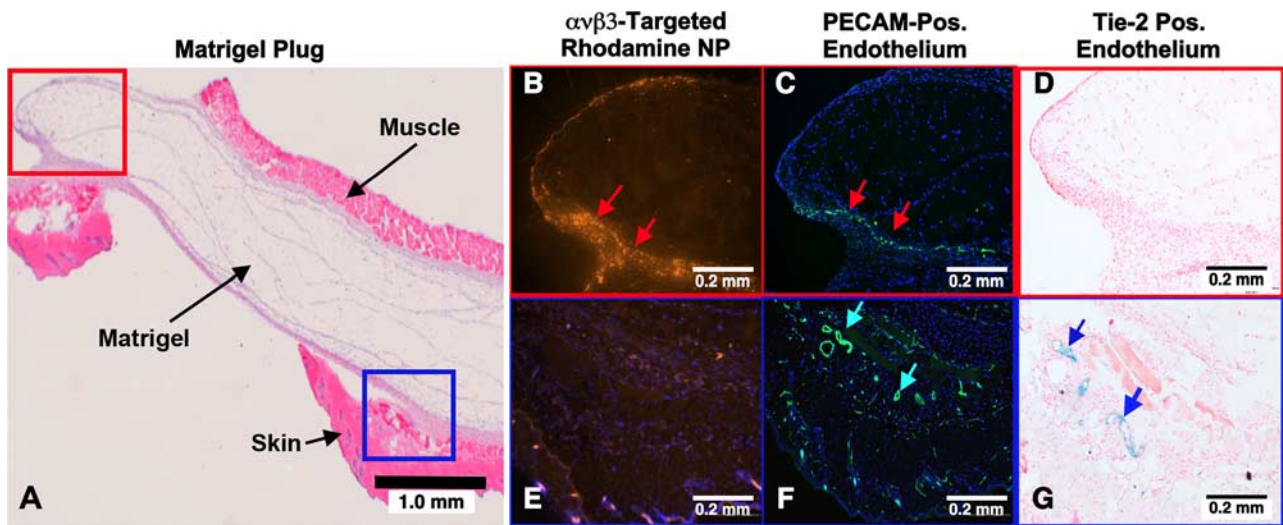


Figure 4. Microscopic examination of FGF Matrigel subcutaneous explant from FVB/N-TgN(TIE2LacZ)182Sato mice following injection (*i.v.*) of $\alpha_v\beta_3$ -targeted rhodamine-labeled GNB nanoparticles. These transgenic mice carry a β -galactosidase reporter gene under the control of the murine Tek (Tie2) promoter. LacZ is expressed specifically in vascular endothelial cells in embryonic and adult mice. A) H&E staining of excised implant, providing spatial orientation of the matrix with respect to skin and muscle. Red box region is further examined in B–D. Blue box region is studied in more detail in E–G. B, E) Accumulation of $\alpha_v\beta_3$ -targeted rhodamine nanoparticles in the red (B) and blue (E) tissue regions. Note the brilliant and dense accumulation of NPs in panel B (red arrows) and little to no accumulation of particles in the panel E. C, F) Staining of vascular endothelium for PECAM (CD34) in the red (C) and blue (F) regions of the Matrigel plug. There is dense vasculature in both locations (red arrows in panel C; turquoise arrows in panel F). D, G) LacZ signal for β -galactosidase under Tie2 promoter control. No LacZ signal is appreciated in panel D, reflecting a paucity of mature microvessels. In contradistinction, there is strong LacZ signal in panel G. These results indicate that the $\alpha_v\beta_3$ -GNB nanoparticles are specifically targeted to angiogenic endothelial cells (PECAM⁺, Tie-2⁻) and not to more mature microvessels, which are PECAM⁺, Tie-2⁺. The data corroborate that PAT imaging with $\alpha_v\beta_3$ -targeted GNBS specifically distinguishes and enhances the angiogenic neovasculature from new but more mature and differentiated microvessels.

Conversely, Tie-2 staining in panel G closely corresponded to the PECAM signal in Fig. 4F, neither of which was associated with rhodamine $\alpha_v\beta_3$ -GNB.

These data indicate that the PA signal observed with $\alpha_v\beta_3$ -GNB was from the forming (PECAM⁺, Tie-2⁻) angiogenic endothelium induced by the Matrigel growth factors and not from mature microvessels (PECAM⁺, Tie-2⁺) in the plug periphery. While PAT alone cannot differentiate PA signal derived from forming and stabilized neovessels, with $\alpha_v\beta_3$ -GNB contrast enhancement, the PAT sensitively discriminates angiogenesis and microvasculature.

DISCUSSION

Angiogenesis is an essential microanatomical biomarker of tumor and cardiovascular disease progression and intensity, as well as a metric of lesion response to therapy. PAT offers a versatile and lower-cost methodology to assess the angiogenic status of cancers, such as head and neck, breast, skin, prostate, uterine, gastrointestinal, and testicular neoplasia, before or after therapy, particularly antiangiogenic treatment, using angiogenesis as the basis of treatment, as a marker of tumor remission, or an indicator of disease recrudescence. The same paradigm applies to carotid or peripheral vascular disease, where angiogenesis is not only a direct intramural marker of plaque inflammatory activity and progression but also an amplifying element leading to lesion instability.

PAT contrast agents have been reported based on dyes (27, 28); gold nanoparticles, nanorods or nanocages (29–33); and single-wall carbon nanotubes (34). Colloidal GNBs have been reported for *in vivo* sentinel lymph node imaging using a sub-100-nm particle to produce maximal PA signal (33). Similar results have been achieved with small-molecular-mass dyes and nanoparticles, such as gold nanocages. However, in the present research, the goal was to target the $\alpha_v\beta_3$ -integrin receptor, a heterodimeric transmembrane glycoprotein, which is sparsely (nanomolar) presented on the luminal aspect of proliferating *vs.* quiescent endothelial cells and is considered an important neovascular biomarker for molecular imaging (35). The effectiveness of a novel $\alpha_v\beta_3$ -GNB to enhance PA contrast of nascent neovasculature was demonstrated *in vivo* in a mouse model of angiogenesis. The success of this platform required robust amplification of PA signal of GNBs when bound to endothelial $\alpha_v\beta_3$ -integrin receptors; the steric constraint of the GNBs to the vasculature by size, precluding interaction binding to nonendothelial cells; and the high binding affinity and specificity of the well-characterized quinolone-derived peptidomimetic homing ligand.

To date, PA contrast agents targeting angiogenesis have been designed around integrin-targeted indocyanine green (ICG)-fluorescent-peptide conjugates (27, 28, 34, 36, 37). Unfortunately, these agents easily diffuse from the neovascular vasculature, where numer-

ous cell types, including macrophages (38), platelets (39), lymphocytes (39), smooth muscle cells (40), and tumor cells (41, 42), express $\alpha_v\beta_3$ -integrin. In the present study, encapsulating thousands of small gold nanoparticles into a GNB PA contrast agent produced a nanoparticle with >150-nm hydrodynamic diameter, which precluded microscopically detectable extravasation beyond the “leaky” neovasculature of the Matrigel plug in the present report. This observation is further supported by other reports using copolymer and nano-emulsion particles (43, 44). Such steric constraint with $\alpha_v\beta_3$ -GNB nanoparticles greatly enhances neovascular specificity, which is essential for quantitative biomedical applications.

A recent study indicates that the upper threshold for bioelimination of solid particles through kidney glomerulae is ~6 nm (45). While hepatic clearance is viable for larger particles in rodents, due to an open biliary canaliculi system (46, 47), this ductile route is unavailable in humans. Individual gold particles can be functionalized and targeted to sparse biosignatures, such as the $\alpha_v\beta_3$ -integrin, but robust signals may only be achieved by increasing particle size well beyond 6 nm. $\alpha_v\beta_3$ -GNBs were designed to achieve robust amplification of the PA signal by entrapping ~2000+ minute gold particles (3–4 nm each) into a single vascular constrained colloidal particle. Thus, GNBs delivered a large gold payload with each binding event; with particle metabolism, the released gold particles were well below the reported renal clearance ceiling.

In the present study, contrast development over time relative to baseline signal was measured as an angiogenesis index, which would require preimaging and post-imaging of patients. Although such an approach is clinically feasible, a more workflow friendly protocol may be to image with PAT at dual frequencies, one optimized for hemoglobin and the other for $\alpha_v\beta_3$ -GNBs, relating each to a specific volume of tumor or carotid wall to obtain an index of angiogenic *vs.* mature vessels per voxel. Further research to refine how to capture the power of PA molecular imaging to discriminate neovasculature from mature vasculature and correlate this relationship to disease progression and response will be essential.

While the present report represents only a first step toward clinical translation of $\alpha_v\beta_3$ -GNBs, the prospects for success from a chemistry, manufacture, and controls perspective are excellent, given the elegance of the process for scale-up. However, other barriers to development currently must be overcome. In particular, PAT is a nascent modality with no clinically installed instrument base. While the results obtained in this research utilized a clinically appropriate acoustic receive frequency (10 MHz), the instrumentation was a laboratory robotic scanner. The first PAT scanners for the preclinical research market are now commercially available, but clinical medical scanners capable of integrating PAT and ultrasound images will be several years more in development. Given the longer time to complete preclinical regulatory requirements for a GNB

investigational new drug (IND) approval than the time required for a the instrument to receive an investigational device exemption (IDE), perhaps the two could be codeveloped to reach the clinic in the same timeframe.

CONCLUSIONS

In this report, we demonstrate the efficacy of $\alpha_v\beta_3$ -targeted GNBs for sensitive and specific angiogenesis imaging in a Matrigel-plug mouse model. Rather than increasing gold particle size to increase PA signal amplification, which could compromise bioelimination, $\alpha_v\beta_3$ -GNBs entrap thousands of gold nanoparticles (2–4 nm) to enhance signals with particles below the reported renal clearance ceiling. The incorporation of high-gold-particle payloads desirably yields a colloid agent of >150 nm, which provided vascular constraint for targeting $\alpha_v\beta_3$ -integrin on angiogenic vascular cells without confounding signals from extravasation and binding to non-endothelial cells expressing this biosignature. In addition to providing a 600% increase in PA angiogenesis index *vs.* the baseline inherent contrast from red blood cell hemoglobin, the homing of the particles and origination of signal was shown to be specific to immature (Tie-2⁻, PECAM⁺) neovessels and not associated with matured (Tie-2⁺, PECAM⁺) microvessels. Moreover, $\alpha_v\beta_3$ -GNBs enabled PAT to detect and quantify developing angiogenic bridges and sprouts undetectable in the baseline images. The combination of PAT and $\alpha_v\beta_3$ -GNBs offers sensitive and specific discrimination and quantification of angiogenesis, which will be clinically applicable to a broad variety of highly prevalent diseases, particularly cancer and cardiovascular disease. FJ

The authors greatly appreciate the financial support from the American Heart Association (grant 0835426N, to D.P.) and the U.S. National Institutes of Health (grants NS059302 and CA119342, to G.M.L.; HL073646, to S.A.W.; and U54 CA136398, R01 EB000712, and R01 EB008085, to L.W.). L.W. has a financial interest in Microphotoacoustics, Inc., and Endra, Inc.; neither provided material, financial, or intellectual support. D.P., G.M.L., M.P., and L.V.W. conceived the research and contributed to the experimental design. D.P. and A.S.P. performed the chemical syntheses, and M.P. performed the PA imaging and postprocessing. J.S.A. and M.P. created and managed the Matrigel rodent model. All authors contributed analysis and interpretation of the data. D.P., M.P., and G.L. wrote the manuscript. All authors read and edited the manuscript.

REFERENCES

1. Li, M. L., Oh, J. T., Xie, X. Y., Ku, G., Wang, W., Li, C., Lungu, G., Stoica, G., and Wang, L. V. (2008) Simultaneous molecular and hypoxia imaging of brain tumors in vivo using spectroscopic photoacoustic tomography. *Proc. IEEE* **96**, 481–489
2. Ku, G., Wang, X., Stoica, G., and Wang, L. V. (2004) Multiple-bandwidth photoacoustic tomography. *Phys. Med. Biol.* **49**, 1329–1338
3. Wang, X., Xie, X., Ku, G., Wang, L. V., and Stoica, G. (2006) Noninvasive imaging of hemoglobin concentration and oxygen-

ation in the rat brain using high-resolution photoacoustic tomography. *J. Biomed. Opt.* **11**, 024015

4. Lungu, G. F., Li, M. L., Xie, X., Wang, L. V., and Stoica, G. (2007) In vivo imaging and characterization of hypoxia-induced neovascularization and tumor invasion. *Int. J. Oncol.* **30**, 45–54
5. Ku, G., Wang, X., Xie, X., Stoica, G., and Wang, L. V. (2005) Imaging of tumor angiogenesis in rat brains in vivo by photoacoustic tomography. *Appl. Opt.* **44**, 770–775
6. Song, L., Maslov, K., Bitton, R., Shung, K. K., and Wang, L. V. (2008) Fast 3-D dark-field reflection-mode photoacoustic microscopy *in vivo* with a 30-MHz ultrasound linear array. *J. Biomed. Opt.* **13**, 054028–054025
7. Brooks, P. C., Clark, R. A. F., and Cheresch, D. A. (1994) Requirement of vascular integrin $\alpha_v\beta_3$ for angiogenesis. *Science* **264**, 569–571
8. Winter, P., Neubauer, A., Caruthers, S., Harris, T., Robertson, J., Williams, T., Schmieder, A., Hu, G., Allen, J., Lacy, E., Wickline, S., and Lanza, G. (2006) Endothelial $\alpha(\nu)\beta_3$ -integrin targeted fumagillin nanoparticles inhibit angiogenesis in atherosclerosis. *Arterioscler. Thromb. Vasc. Biol.* **26**, 2103–2109
9. Winter, P. M., Schmieder, A. H., Caruthers, S. D., Keene, J. L., Zhang, H., Wickline, S. A., and Lanza, G. M. (2008) Minute dosages of $\alpha(\nu)\beta_3$ -targeted fumagillin nanoparticles impair Vx-2 tumor angiogenesis and development in rabbits. *FASEB J.* **22**, 2758–2767
10. Wang, X. D., Pang, Y. J., Ku, G., Xie, X. Y., Stoica, G., and Wang, L. V. (2003) Noninvasive laser-induced photoacoustic tomography for structural and functional in vivo imaging of the brain. *Nat. Biotech.* **21**, 803–806
11. Siphanto, R. I., Thumma, K. K., Kolkman, R. G., van Leeuwen, T. G., de Mul, F. F., van Neck, J. W., van Adrichem, L. N., and Steenbergen, W. (2005) Serial noninvasive photoacoustic imaging of neovascularization in tumor angiogenesis. *Opt. Express.* **13**, 89–95
12. Siphanto, R. I., Kolkman, R. G., Huisjes, A., Pilatou, M. C., de Mul, F. F., Steenbergen, W., and van Adrichem, L. N. (2004) Imaging of small vessels using photoacoustics: an in vivo study. *Lasers Surg. Med.* **35**, 354–362
13. Maslov, K., Zhang, H. F., Hu, S., and Wang, L. V. (2008) Optical-resolution photoacoustic microscopy for in vivo imaging of single capillaries. *Optics Lett.* **33**, 929–931
14. Lao, Y., Xing, D., Yang, S., and Xiang, L. (2008) Noninvasive photoacoustic imaging of the developing vasculature during early tumor growth. *Phys. Med. Biol.* **53**, 4203–4212
15. Zhang, E. Z., Laufer, J. G., Pedley, R. B., and Beard, P. C. (2009) In vivo high-resolution 3D photoacoustic imaging of superficial vascular anatomy. *Phys. Med. Biol.* **54**, 1035–1046
16. Jose, J., Manohar, S., Kolkman, R. G., Steenbergen, W., and van Leeuwen, T. G. (2009) Imaging of tumor vasculature using Twente photoacoustic systems. *J. Biophotonics* **2**, 701–717
17. Hu, S., Oladipupo, S., Yao, J., Santeford, A. C., Maslov, K., Kovalski, J., Arbeit, J. M., and Wang, L. V. (2010) Optical-resolution photoacoustic microscopy of angiogenesis in a transgenic mouse model. *Proc. SPIE* **7564**, 756406
18. Meoli, D. F., Sadeghi, M. M., Krassilnikova, S., Bourke, B. N., Giordano, F. J., Dione, D. P., Su, H., Edwards, D. S., Liu, S., Harris, T. D., Madri, J. A., Zaret, B. L., and Sinusas, A. J. (2004) Noninvasive imaging of myocardial angiogenesis following experimental myocardial infarction. *J. Clin. Invest.* **113**, 1684–1691
19. Miyauchi, A., Alvarez, J., Greenfield, E. M., Teti, A., Grano, M., Colucci, S., Zamboni-Zallone, A., Ross, F. P., Teitelbaum, S. L., Cheresch, D. (1991) Recognition of osteopontin and related peptides by an $\alpha_v\beta_3$ integrin stimulates immediate cell signals in osteoclasts. *J. Biol. Chem.* **266**, 20369–20374
20. Song, K. H. and Wang, L. H. V. (2007) Deep reflection-mode photoacoustic imaging of biological tissue. *J. Biomed. Opt.* **12**, 060503
21. Maslov, K., Stoica, G. and Wang, L. V. H. (2005) In vivo dark-field reflection-mode photoacoustic microscopy. *Opt. Lett.* **30**, 625–627
22. Laser Institute of America (2000) *American National Standard for Safe Use of Lasers ANSI Z136.1-2000*, American National Standards Institute, New York
23. Fathers, K. E., Stone, C. M., Minhas, K., Marriott, J. J., Greenwood, J. D., Dumont, D. J., and Coomber, B. L. (2005) Heterogeneity of Tie2 expression in tumor microcirculation: influ-

- ence of cancer type, implantation site, and response to therapy. *Am. J. Pathol.* **167**, 1753–1762
24. Imhof, B. A., and Aurrand-Lions, M. (2006) Angiogenesis and inflammation face off. *Nat. Med.* **12**, 171–172
 25. Winter, P. M., Caruthers, S. D., Kassner, A., Harris, T. D., Chinen, L. K., Allen, J. S., Lacy, E. K., Zhang, H., Robertson, J. D., Wickline, S. A., and Lanza, G. M. (2003) Molecular imaging of angiogenesis in nascent Vx-2 rabbit tumors using a novel alpha(nu)beta3-targeted nanoparticle and 1.5 Tesla magnetic resonance imaging. *Cancer Res.* **63**, 5838–5843
 26. Schmieder, A., Winter, P., Caruthers, S., Harris, T., Williams, T., Allen, J., Lacy, E., Zhang, H., MJ, S., Wickline, S., and Lanza, G. (2005) MR molecular imaging of melanoma angiogenesis with avb3-Targeted paramagnetic nanoparticles. *Magn. Reson. Med.* **53**, 621–627
 27. Wang, L. V., Xie, X., Oh, J. T., Li, M. N., Ku, G., Ke, S., Similache, S., Li, C., and Stoica, G. (2005) Combined photoacoustic and molecular fluorescence imaging in vivo. *IEEE Eng. Med. Biol. Proc.* **7**, 190–192
 28. Xie, X., Oh, J. T., Li, M. L., Ku, G., Wang, X., Ke, S., Li, C., Similache, S., Stoica, G., and Wang, L. V. (2005) Photoacoustic tomography and molecular fluorescence imaging: Dual modality imaging of small animal brains in vivo. *Proc. SPIE* **5697**, 107–110
 29. Yavuz, M. S., Cheng, Y., Chen, J., Cobley, C. M., Zhang, Q., Rycenga, M., Xie, J., Kim, C., Song, K. H., Schwartz, A. G., Wang, L. V., and Xia, Y. (2009) Gold nanocages covered by smart polymers for controlled release with near-infrared light. *Nat. Mater.* **8**, 935–939
 30. Cho, E. C., Kim, C., Zhou, F., Cobley, C. M., Song, K. H., Chen, J., Li, Z. Y., Wang, L. V., and Xia, Y. (2009) Measuring the optical absorption cross sections of Au-Ag nanocages and Au nanorods by photoacoustic imaging. *J. Phys. Chem. C. Nanomater. Interfaces* **113**, 9023–9028
 31. Song, K. H., Kim, C., Cobley, C. M., Xia, Y., and Wang, L. V. (2009) Near-infrared gold nanocages as a new class of tracers for photoacoustic sentinel lymph node mapping on a rat model. *Nano. Lett.* **9**, 183–188
 32. Pan, D., Pramanik, M., Senpan, A., Yang, X., Song, K. H., Scott, M. J., Zhang, H., Gaffney, P. J., Wickline, S. A., Wang, L. V., and Lanza, G. M. (2009) Molecular photoacoustic tomography with colloidal nanobeacons. *Angew. Chem. Int. Ed. Engl.* **48**, 4170–4173
 33. Pan, D., Pramanik, M., Senpan, A., Ghosh, S., Wickline, S. A., Wang, L. V., and Lanza, G. M. (2010) Near infrared photoacoustic detection of sentinel lymph nodes with gold nanobeacons. *Biomaterials* **31**, 4088–4093
 34. De la Zerda, A., Zavaleta, C., Keren, S., Vaithilingam, S., Bodapati, S., Liu, Z., Levi, J., Smith, B. R., Ma, T. J., Oralkan, O., Cheng, Z., Chen, X., Dai, H., Khuri-Yakub, B. T., and Gambhir, S. S. (2008) Carbon nanotubes as photoacoustic molecular imaging agents in living mice. *Nat. Nanotechnol.* **3**, 557–562
 35. Schmieder, A. H., Caruthers, S. D., Zhang, H., Williams, T. A., Robertson, J. D., Wickline, S. A., Lanza, G. M. (2008) Three-dimensional MR mapping of angiogenesis with alpha5beta1(alpha nu beta3)-targeted theranostic nanoparticles in the MDA-MB-435 xenograft mouse model. *FASEB J.* **22**, 4179–4189
 36. Xie, X., Li, M. L., Oh, J. T., Ku, G., Wang, W., Li, C., Similache, S., Lungu, G. F., Stoica, G., and Wang, L. V. (2006) Photoacoustic molecular imaging of small animals in vivo. *Proc. SPIE* **6086**, 608606
 37. Xiang, L., Yuan, Y., Xing, D., Ou, Z., Yang, S., and Zhou, F. (2009) Photoacoustic molecular imaging with antibody-functionalized single-walled carbon nanotubes for early diagnosis of tumor. *J. Biomed. Opt.* **14**, 021008
 38. De Nichilo, M., Burns, G., and (1993) Granulocyte-macrophage and macrophage colony-stimulating factors differentially regulate alpha v integrin expression on cultured human macrophages. *Proc. Natl. Acad. Sci. U. S. A.* **90**, 2517–2521
 39. Helluin, O., Chan, C., Vilaire, G., Mousa, S., DeGrado, W. F., and Bennett, J. S. (2000) The activation state of alphavbeta 3 regulates platelet and lymphocyte adhesion to intact and thrombin-cleaved osteopontin. *J. Biol. Chem.* **275**, 18337–18343
 40. Itoh, H., Nelson, P., Mureebe, L., Horowitz, A., and Kent, K. (1997) The role of integrins in saphenous vein vascular smooth muscle cell migration. *J. Vasc. Surg.* **25**, 1061–1069
 41. Carreiras, F., Denoux, Y., Staedel, C., Lehmann, M., Sichel, F., and Gauduchon, P. (1996) Expression and localization of alpha v integrins and their ligand vitronectin in normal ovarian epithelium and in ovarian carcinoma. *Gynecol. Oncol.* **62**, 260–267
 42. Kageshita, T., Hamby, C. V., Hirai, S., Kimura, T., Ono, T., and Ferrone, S. (2000) Differential clinical significance of alpha (v) Beta(3) expression in primary lesions of acral lentiginous melanoma and of other melanoma histotypes. *Int. J. Cancer* **89**, 153–159
 43. Hu, G., Lijowski, M., Zhang, H., Partlow, K. C., Caruthers, S. D., Kiefer, G., Gulyas, G., Athey, P., Scott, M. J., Wickline, S. A., and Lanza, G. M. (2007) Imaging of Vx-2 rabbit tumors with alpha(nu)beta3-integrin-targeted 111In nanoparticles. *Int. J. Cancer* **120**, 1951–1957
 44. Weissleder, R., Bogdanov, A., Jr., Tung, C. H., and Weinmann, H. J. (2001) Size optimization of synthetic graft copolymers for in vivo angiogenesis imaging. *Bioconjug. Chem.* **12**, 213–219
 45. Choi, H. S., Liu, W., Liu, F., Nasr, K., Misra, P., Bawendi, M. G., and Frangioni, J. V. (2010) Design considerations for tumour-targeted nanoparticles. *Nat. Nanotechnol.* **5**, 42–47
 46. Dupas, B., Pradal, G., Muller, R. N., Bonnemain, B., Meflah, K., and Bach-Gansmo, T. (2001) Hepatocyte-mediated transport to the bile of AMI-HS, a particulate contrast agent. *Invest. Radiol.* **36**, 509–517
 47. Hu, J., Zhang, X., Dong, X., Collins, L., Sawyer, G. J., and Fabre, J. W. (2005) A remarkable permeability of canalicular tight junctions might facilitate retrograde, non-viral gene delivery to the liver via the bile duct. *Gut* **54**, 1473–1479

Received for publication September 2, 2010.

Accepted for publication November 4, 2010.